nature plants

ARTICLES

https://doi.org/10.1038/s41477-019-0497-6

Tissue-specific accumulation of pH-sensing phosphatidic acid determines plant stress tolerance

Wenyu Li[1], Tengzhao Song[1], Lukas Wallrad[2], Jörg Kudla[2], Xuemin Wang[3,4] and Wenhua Zhang[1*]

The signalling lipid phosphatidic acid (PA) is involved in regulating various fundamental biological processes in plants. However, the mechanisms of PA action remain poorly understood because currently available methods for monitoring PA fail to determine the precise spatio-temporal dynamics of this messenger in living cells and tissues of plants. Here, we have developed PAleon, a PA-specific optogenetic biosensor that reports the concentration and dynamics of bioactive PA at the plasma membrane based on Förster resonance energy transfer (FRET). PAleon was sensitive enough to monitor physiological concentrations of PA in living cells and to visualize PA dynamics at subcellular resolution in tissues when they were challenged with abscisic acid (ABA) and salt stress. PAleon bioimaging revealed kinetics and tissue specificity of salt stress-triggered PA accumulation. Compared with wild-type *Arabidopsis*, the *pldα1* mutant lacking phospholipase Dα1 (PLDα1) for PA generation showed delayed and reduced PA accumulation. Comparative analysis of wild type and *pldα1* mutant indicated that cellular pH-modulated PA interaction with target proteins and PLD/PA-mediated salt tolerance. Application of the PA biosensor PAleon uncovered specific spatio-temporal PA dynamics in plant tissues. Our findings suggest that PA signalling integrates with cellular pH dynamics to mediate plant response to salt stress.

Phosphatidic acid (PA) serves as a precursor for the synthesis of glycerol-phospholipids and triacylglycerol. In addition, PA functions as an important signalling lipid involved in regulating various fundamental cellular functions, including vesicular trafficking, secretion, endocytosis, immune activation, pH sensing, and hormonal and stress responses in eukaryotic cells[1–4]. In the plant kingdom, prominent examples are the PA-mediated regulation of stomatal movement and drought and salt stress responses[5–11]. Many pathways, such as phospholipase D (PLD)-mediated hydrolysis of phospholipids, phosphorylation of diacylglycerol (DAG) by DAG-kinase (DGK) and acylation of lysoPA by lysoPA acyltransferases, contribute to the formation of cellular PA pools[3,12]. PA function in signal transduction in response to various environmental and internal cues is brought about by its direct interaction with effector proteins, such as protein kinases, phosphatases, phospholipases, transcription factors, NADPH oxidases and microtubule-associated proteins, modulating their activity[3]. The simultaneous function of PA as a 'structural component' and 'signalling molecule' has hampered deciphering its specific functions in cellular signalling and regulatory processes.

Initial evidence for dynamic increases of PA accumulation, for example in response to salt or drought stress, was obtained using radioisotope labelling, chromatographic techniques and mass spectrometric methods[13–16]. However, these approaches could not identify the bioactive fraction of the cellular PA and did not provide spatial information about its accumulation. To gain insights into the localization and dynamics of PA pools in living cells, PA-specific probes have been developed although the number of available probes was rather limited[4]. The N-terminal PA-binding domain of yeast SNARE protein Spo20p[17] and the PA-binding domain of mammalian Raf1 kinase[18] have been most widely used. In plants, Potocký et al.[19] used a biosensor that consisted of the Spo20p–PA-binding domain fused to fluorescent proteins. With this biosensor, PA was found to mark a distinct subapical region of the plasma membrane (PM) in tobacco pollen tubes and to show a high rate of turnover during pollen elongation[19]. More recently, additional Spo20p-based PA biosensors with an extra nuclear export signal were developed, namely mCIT-1×PASS and mCIT-2×PASS[20]. These sensors were found on the flank region of growing root hairs, in a pattern resembling that of PA sensors in growing tobacco pollen tubes[19,20]. PA accumulates in the cytosolic leaflet of the plant PM and contributes to surface charges[20]. These PA probes in plants rely on membrane translocation of the probe and a single fluorescence signal.

Potential problems associated with translocation-dependent fluorescent protein-tagged PA probes include the difficulty of controlling the concentration and localization of the probe. A too high or low level of probes may affect their translocation from the cytosol to the PM or endomembranes. In addition, the effects of probe concentration and photobleaching are difficult to control. A single fluorescence signal does not discriminate between PA increases and changes in the thickness of the cell or membrane ruffling events, which would also affect fluorescence[21]. Moreover, translocation-dependent PA sensors cannot be targeted, hampering the study of PA fluctuations in specific subcellular membranes. Targeting the PA detection to specific membranes is crucial because the critical micelle concentration of PA is much lower than that of cellular PA, so changes in cellular PA mainly affect membrane-associated PA[22]. The cellular level of PA in *Arabidopsis*

[1]College of Life Sciences, State Key Laboratory of Crop Genetics and Germplasm Enhancement, Nanjing Agricultural University, Nanjing, China. [2]Institut für Biologie und Biotechnologie der Pflanzen, Universität Münster, Münster, Germany. [3]Department of Biology, University of Missouri, St Louis, MO, USA. [4]Donald Danforth Plant Science Center, St Louis, MO, USA. *e-mail: whzhang@njau.edu.cn

is estimated to be around 50–100 µM under normal growth conditions[23]. In addition, small local changes in signalling PA may be hard to detect with translocation-dependent PA probes because PA is a central intermediate for the synthesis of glycerolipids, such as phospholipids, galactolipids and triacylglycerol, and there are large PA pools for glycerolipid metabolism.

To circumvent the challenges associated with single fluorescent PA probes, PA probes based on Förster resonance energy transfer (FRET) have been developed to monitor PA dynamics in mammalian and yeast cells[4,24]. FRET sensors based on ratio imaging have intrinsic advantages over single-intensity sensors. For instance, potential effects of probe concentration variation or photobleaching are abrogated due to the ratiometric procedures. Also, FRET sensors for PA can be targeted to specific cellular subdomains to measure local changes of PA. Here, we report the development of the FRET-based PA biosensor PAleon and use of this tool to explore PA function in plant stress responses.

Results

Designing a ratiometric plant PA biosensor. In previous work, we discovered PA as a central lipid-signalling molecule in abscisic acid (ABA)-mediated guard cell regulation and identified the NADPH oxidase RBOHD as an important effector target of PA function[7]. PA binding to RBOHD was mapped to its N-terminal cytoplasmic domain and four Arg residues (149, 150, 156, 157) were found to be essential for PA binding and PA-dependent activation of RBOHD. The selectivity and specificity of PA–RBOHD binding have been confirmed using co-sedimentation assay, enzyme-linked immunosorbent assay (ELISA) and filter binding[7]. To create a PA-specific ratiometric plant biosensor, we cloned the PA-binding domain of RBOHD, encompassing amino acids 1–250 (designated as R250) but lacking the Ca^{2+}-binding EF-hands and G protein-binding domain, into an expression vector and then purified recombinant R250 protein. As a control, we generated an R250M protein in which the four PA-binding Arg residues were replaced by Ala[7] (Fig. 1a,b). In vitro binding assays confirmed that R250, but not R250M, specifically bound synthetic PA species and natural PA. Both proteins did not interact with other lipids tested, including phosphatidylcholine (PC), phosphatidylethanolamine (PE), phosphatidylglycerol (PG), phosphatidylinositol (PI), phosphatidylserine (PS), DAG or phosphoinositides (Supplementary Fig. 1a). Isothermal titration calorimetry indicated that a PA species, 16:0–18:2 PA (acyl compositions were 16:0–18:2 fatty acids), increased by salt and ABA[7,25], interacted with R250 at an approximate ratio of 2:1 with a dissociation constant of 2.3 µM (Fig. 1c), a PA concentration lower than in *Arabidopsis* cells[23,26]. Another PA species, di 16:0 PA, showed a much lower binding to R250, identical with the results of overlay assays (Fig. 1c and Supplementary Fig. 1a). In addition, R250M showed a much lower affinity towards PA (16:0–18:2; Fig.1c), indicating that R250 and R250M would provide suitable PA-sensing and specificity control domains, respectively, for an effective PA biosensor. To create this high-affinity PA biosensor and low-affinity control, R250 or R250M was inserted between a cyan fluorescent protein (CFP) and a VENUS fast maturing yellow fluorescent protein. The functional modules of this reporter protein were interconnected by flexible linkers. The C-terminal K-Ras4B farnesylation signal[24] was used as a PM-targeting sequence. The resulting FRET-based biosensor with the R250 domain is named PAleon whereas that with the R250M is named m-PAleon (Fig. 1a).

To address the functionality of PAleon, a control for acceptor bleaching was performed using *Arabidopsis* protoplasts containing PAleon. Three regions of interest (ROIs) were selected from a PAleon-expressing protoplast (Supplementary Fig. 2). ROI 1 (bleaching) and ROI 2 (no bleaching) were located on the PM, while ROI 3 (bleaching) was located in the cytosol. After bleaching for 2 min, the VENUS signal was bleached in ROI 1, while the CFP signal was increased in the same region. The signal intensity of VENUS or CFP in ROI 2 was not changed during the observation and that in ROI 3 was not changed after bleaching (Supplementary Fig. 2). These results confirmed that the FRET occurred between CFP and VENUS.

We subsequently generated transgenic lines of *Arabidopsis* (Col-0) expressing PAleon (or m-PAleon) under the control of constitutive promoters[27]. Seven independent PAleon-expressing lines were obtained and initial experiments showed a FRET increase of PAleon in response to 50 µM ABA treatment (Supplementary Fig. 3). Further observation of transgenic lines revealed that PAleon was ubiquitously expressed in all plant tissues, including leaves, guard cells, hypocotyl, stem and roots (Supplementary Fig. 4e–i). PAleon was co-localized with the PM marker dye FM4-64, indicating PM targeting of the PA biosensor (Supplementary Fig. 4b–d). PAleon- or m-PAleon-expressing plants showed no discernable morphological or developmental differences from wild-type (WT). In addition, those plants showed identical responsiveness to ABA in terms of ABA-inhibited root growth and all analysed plants showed identical responsiveness, suggesting that biosensor expression did not interfere with plant physiology and stress responsiveness (Supplementary Fig. 5).

PAleon reports PA dynamics in plants. We next addressed the functionality of the PAleon biosensor in planta by performing live cell PA imaging using spinning disc confocal laser microscopy. Four-day-old *Arabidopsis* seedlings were fixed in a perfusion chamber that allowed rapid exchange of application solutions[20]. We initially imposed a buffer exchange from 0 to 50 µM PA and defined the root maturation zone as the ROI. The resulting FRET efficiency indicative for PA accumulation was determined as ratio value (R) calculated by dividing the emission intensity of VENUS by the emission intensity of CFP at defined time points (VENUS/CFP, normalized to the initial ratio R_0 and plotted versus time, $\Delta R/R_0$). Consequently, the ratio value is proportional to the concentration of PA that efficiently binds to the PAleon biosensor. Application of 50 µM natural PA (Fig. 2a) or 16:0–18:2 PA (Fig. 2b) to PAleon-expressing plants resulted in a rapid and dramatic increase of $\Delta R/R_0$ initiating about 500 s after onset of exposure (Fig. 2). In contrast, similar treatments of m-PAleon-expressing plants only induced minor baseline noise (Supplementary Fig. 6a). This result establishes the PA-responsiveness of PAleon in vivo and suggests that the delay in response time reflects the uptake kinetics of exogenously applied PA.

Subsequent application of other phospholipids, including PC, DAG, PE, PI and PG, did not result in any discernable increase of $\Delta R/R_0$, while application PS produced a minor response in $\Delta R/R_0$ (Fig. 2a and Supplementary Fig. 6b). We next determined the PAleon response to PtdIns4P and PtdIns(4,5)P_2, which are also anionic phospholipids but have more negative charges in the head group than does PA[20,28]. PtdIns4P or PtdIns(4,5)P_2 did not induce increase of $\Delta R/R_0$; instead they induced a slight decrease of $\Delta R/R_0$ (Supplementary Fig. 6c). The deletion of PtdIns4P generation using the phenylarsine oxide (PAO), an inhibitor of PtdIns 4-kinase[28], did not notably affect PAleon presence at the PM (Supplementary Fig. 7). In addition, the PA species di 16:0, which has been detected in animals and yeast but appears to be absent in *Arabidopsis*[7] and exhibited a negligible binding to PAleon in vitro (Fig. 1c), did not trigger a detectable PA response (Supplementary Fig. 6d). Finally, we investigated the dose-dependent response of PAleon by applying varied concentrations of 16:0–18:2 PA and observed a positive quantitative correlation that did not appear to reach saturation of the biosensor during our data acquisition time of 30 min (Fig. 2b–g). Together, these results indicate that PAleon is a sensitive and quantitative biosensor at the PM in living plant tissues, specifically responding to exogenously added PA.

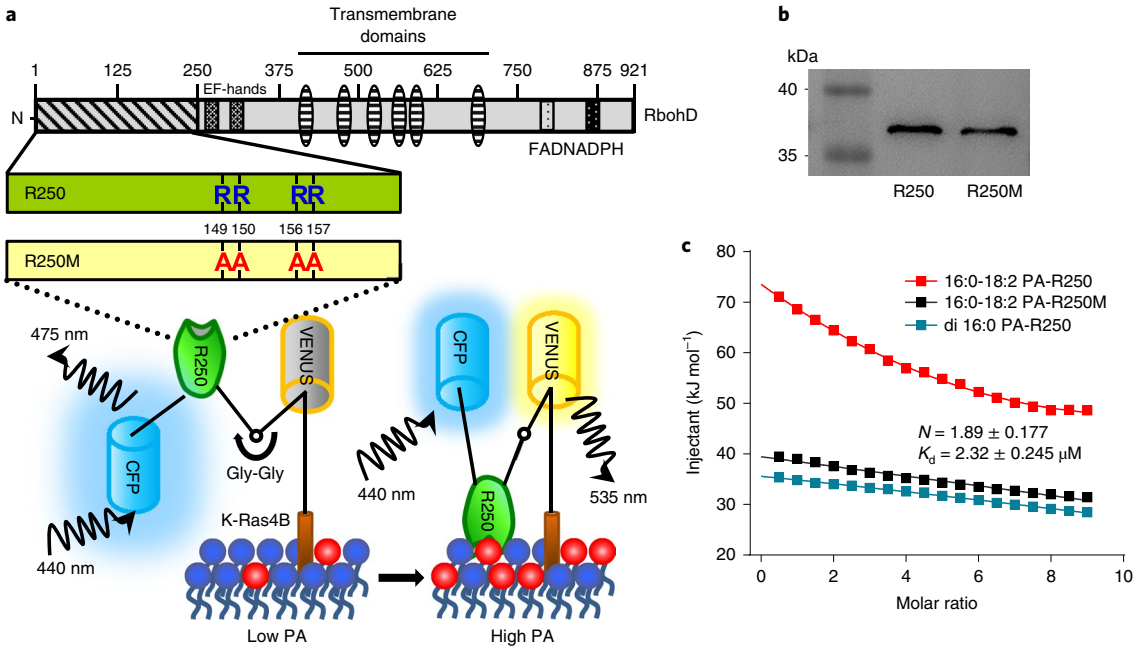

Fig. 1 | Design of PA biosensor. a, Schematic representations of the FRET-based PA biosensor (PAleon). The domain between CFP and VENUS was derived from RbohD and bound to PA selectively (R250). The quadruple mutation (R250M) caused R250 to lose the ability to bind PA and was used as a negative control. K-Ras4B at the C-terminal region was used to anchor PAleon at the PM. After binding of increased PA to R250 in the PAleon biosensor, a flipflop-type conformational change occurred, decreasing the distance and changing the orientation between the fluorescent proteins and thereby increasing the efficiency of FRET from CFP to VENUS. **b**, Purification of R250 and R250M recombinant proteins tagged with His is shown. Western blots are representative of six experiments giving similar results. **c**, PA binding to R250 and R250M measured by isothermal titration calorimetry is shown. The value is integration of the peaks corresponding to each injection, according to Origin-based software provided by the manufacturer. For each injection, PA solution was titrated into a sample cell containing R250 or R250M. PA with fatty acid chains palmitoyl-linoleoyl (16:0–18:2) or dipalmitoyl (di 16:0) was used for R250 or R250M binding. The binding stoichiometry (N), dissociation constant (K_d) and their errors, which are for 16:0–18:2 PA–R250 binding, were measured by Origin software according to fitting curves. No specific binding was detected for 16:0–18:2 PA–R250M or di 16:0 PA–R250. Representative data from three independent experiments with similar results are shown.

PAleon reveals PA dynamics in response to ABA. The above experiments that used lipids exogenously applied could not fully rule out the possibility that applied PA might be modified when taken up by plants. Therefore, we sought to detect PA changes by PAleon in plants under stress conditions that were known to increase PA production. Our previous work showed that ABA induced an increase in PA in planta but the PA dynamics and subcellular distributions remain unknown[6,7]. Since guard cells represent an excellent single-cell model system for studying the dynamics of signalling molecules in plants, we focused our initial in vivo PA monitoring efforts on this cell type. Application of 100 μM ABA induced a discernable increase in $\Delta R/R_0$ indicative for PA accumulation in 200 s, which reached stable saturation 300 s after application (Fig. 3a,b). These results support the notion that PAleon reliably and quantitatively visualizes the dynamic accumulation of PA at the PM in response to hormonal cues in guard cells. Since the stomata in these analyses were still open at the end of data acquisition (760 s; Fig. 3b), these findings also indicate that ABA-induced PA accumulation precedes stomatal closure.

We next investigated ABA-induced PA accumulation in roots, using the maturation root zone as ROI. Seedlings were incubated in imaging buffer for calibration for several minutes and in 60–90 s after onset of 100 μM ABA application, we detected a rapid rise in $\Delta R/R_0$ that reached a saturated level in about 5 min (Fig. 3c,d). The increase of $\Delta R/R_0$ was dependent on the application of ABA concentration from 1 to 100 μM (Fig. 3c). To corroborate that an increase in PA was causative for the observed increase in $\Delta R/R_0$, we pursued a pharmacological approach by using *n*-butanol as a suppressor of PA production. *n*-Butanol decreases PA production derived from PLD by competing with H_2O as hydroxyl donor to the phosphatidyl moiety[3]. We first applied ABA alone and then added *n*-butanol (0.4%, v/v) into the ABA flux solution at the beginning of maximal PA accumulation. This treatment prompted an immediate decrease of $\Delta R/R_0$ and pushed the $\Delta R/R_0$ almost back to basal level in about 500 s (Fig. 3e). To exclude a possible non-specific toxic effect of *n*-butanol, we applied the same concentration of *t*-butanol, an *n*-butanol isomer that does not inhibit PLD-derived PA production and observed only a minor reduction of PA accumulation (Fig. 3f). These results indicate that PLD generates the bioactive PA in response to ABA, that this PA pool is turned over rapidly, and that the rate of PA production by PLD determines the steady-state concentration of signalling PA.

Salt stress triggers tissue-specific patterns of PA accumulation in roots. We next sought to address the spatio-temporal dynamics of PA in response to salt stress as a naturally occurring abiotic cue in roots. Since roots are complex organs with highly differentiated cell types, it would be informative to explain differentiated PA-accumulation patterns that may be indicative for diverse functions of PA in distinct cell types. A confocal microscope was therefore used in tile-scanning mode to capture a whole-organ image of PA dynamics. Rapid stimulus-triggered PA accumulation was observed throughout in a root after application of 100 mM NaCl (Supplementary Fig. 8). To increase the resolution of analyses, we defined three distinct ROIs encompassing root tip (ROI 1), differentiation zone (ROI 2) and maturation zone (ROI 3). Parallel inspection of all three ROIs revealed that PA accumulation occurred with a similar velocity but to a different degree in these three zones (Fig. 4a,b).

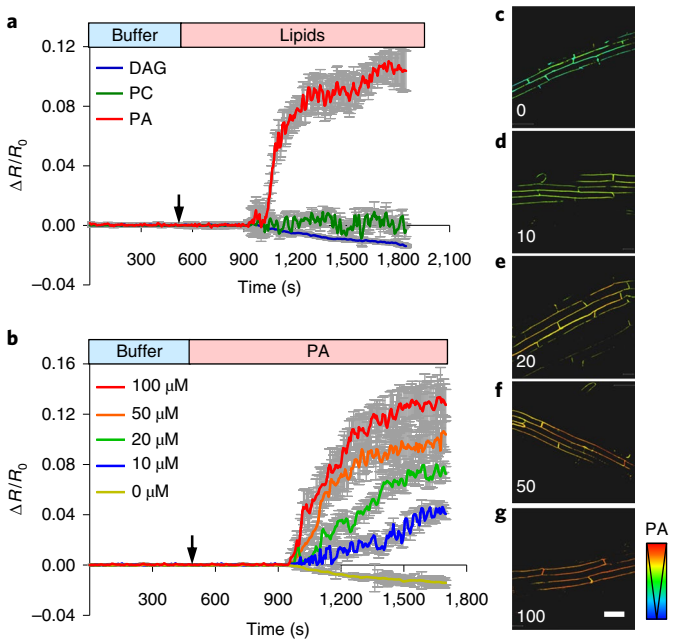

Fig. 2 | PAleon specifically responds to PA based on FRET principles. **a**,**b**, PA monitoring in the maturation zones in the roots of WT *Arabidopsis* seedlings expressing PAleon. Seedlings were challenged with different lipid stimuli for the indicated times and data were analysed with a spinning disc confocal. Traces represent the normalized ratios $\Delta R/R_0$ that were measured from $n = 12$ cells in a seedling and $n = 5$ biologically independent seedlings were observed for each treatment. Data are reported as mean ± s.e. Three independent experiments were done with similar results. In **a**, 50 μM natural lipids was used. In **b**, 16:0–18:2 PA was used. The arrows indicate the addition of lipids. **c**–**g**, The representative images from **b** at 1,700 s. Scale bar, 20 μm.

The salt-induced PA increase was the highest in the root tip, intermediate in the maturation zone and lowest in the differentiation zone (Fig. 4a,c). *n*-Butanol treatment efficiently inhibited PA accumulation in all three zones to near basal levels, indicating a notable contribution of PLD activity to salt-induced PA generation (Fig. 4a and Supplementary Fig. 8). In comparison, the mutated PAleon (m-PAleon) did not show FRET increase when seedlings were exposed to salt stress (or ABA) treatments (Supplementary Fig. 9). These results point to a spatial difference in PA accumulation in roots that deserves further study.

Loss of PLDα1 function delays and impairs stress-induced PA accumulation in roots. Previous studies established phospholipase Dα1 (PLDα1) function in ABA regulation of guard cells and in salt tolerance in *Arabidopsis*, and *pldα1* loss-of-function mutants showed increased drought and salt sensitivity compared to WT[15,23,29]. So we transformed PAleon into *pldα1* lines to investigate the effect of PLDα1 on PA dynamics under stress conditions. We first focused on salt-triggered (100 mM NaCl) accumulation of PA in the maturation zone. While in WT, salt stress again induced an almost immediate rise in PA that within a few seconds reached near-saturation levels, this response was clearly delayed and less pronounced in the *pldα1* mutant, indicating that this enzyme contributes substantially to salt stress-triggered PA generation at the PM (Fig. 5a). We next applied isotonic concentrations of mannitol (200 mM) as non-ionic equivalent for the osmotic stress imposed by 100 mM NaCl. In WT, this treatment induced PA accumulation with similar speed but only reached about 60% of maximum when compared with NaCl treatment (Fig. 5a,b). In *pldα1* mutants, we observed a PA response that was distinct from that to NaCl. In the mutant, mannitol triggered PA accumulation only after a long delay of 300 s and the maximal accumulation never reached 50% of that in WT. These differences observed in the *pldα1* mutant point to potentially interesting but so far unappreciated differential contributions of PLDα1 to osmotic or ionic stress responses. We next determined ABA-triggered (100 μM) accumulation of PA in the maturation zone. In WT plants, we observed a rapid and robust accumulation of PA, while that in the *pldα1* mutant was severely delayed by about 120 s and at maximum reached 50% of the intensity recorded in WT (Fig. 5c). Overall, our data reveal a remarkable temporal complexity of PLDα1-derived PA dynamics that appears to be highly stress-specific.

PA functions as pH sensor for salt tolerance of plants. PA is an anionic lipid consisting of a negatively charged phosphomonoester head group attached to a DAG backbone and exerts its signalling function by direct interaction with PA-binding domains of effector proteins[3]. Importantly, changes in intracellular pH would modulate the protonation of its phosphomonoester and, in this way, modify the electrostatic interactions with the effectors. Accordingly, PA signalling can be fine-tuned by cellular pH, thus PA has a role as a pH biosensor, coupling changes in pH to intracellular signalling pathways at least in yeast[2]. In plants, pH fluctuations occur under salt stress and a pH gradient across the PM, generated by P-type H^+-ATPases, is essential for the Na^+/H^+ antiport to reduce Na^+ in cells[25,30]. Therefore, we sought to investigate if PA functions as a pH sensor in plants and how pH and PA signalling interact during salt stress responses. We first studied if and how pH conditions modulate the salt sensitivity of WT and *pldα1* mutant plants. Seedlings of both lines were cultivated on media ranging from pH 4.5 to 7 with or without 100 mM NaCl. Consistent with previous results[25], the *pldα1* mutant displayed sensitivity to salt stress at normal pH conditions (pH 5.8; Fig. 6a and Supplementary Fig. 10). On further increase of pH, both WT and the *pldα1* mutant showed decreased root growth. However, under these conditions the sensitivity phenotype of the *pldα1* mutant became increasingly more severe than that of WT plants (Fig. 6a,b and Supplementary Fig. 10). This difference was not observed when WT and *pldα1* were grown under various pH conditions in the absence of NaCl (Supplementary Fig. 10). These results reveal a pH-dependent component of plant salt tolerance that is specifically conveyed by PLDα1.

To address the potential pH-sensing function of PA, we monitored PA changes in plants exposed to different pH. When pH was changed from 5.8 (control) to 4.5, $\Delta R/R_0$ for PA decreased. Conversely, changing pH back to 5.8 resulted in the recovery of the $\Delta R/R_0$, however, to a lower level (Fig. 6c). In addition, if pH was changed from 5.8 to 7.0, $\Delta R/R_0$ for PA increased (Fig. 6d). To determine whether the external pH changes affected the intracellular pH, we used the ratiometric pH indicator 2,7-bis-(2-carboxyethyl)-5-(and-6)-carboxyfluorescein (BCECF) acetoxymethyl ester (AM)[31] and calibrated the [pH]cyt (Supplementary Fig. 11a). Change of external solution pH from 5.8 to 4.5 decreased [pH]cyt by about 0.55 in about 12 min (at 1,200 s), followed by a partial recovery when external pH was restored to pH 5.8 (Supplementary Fig. 11b). Salt stress combined with low pH treatment led to a more pronounced [pH]cyt decrease (~0.7 at 1,200 s). In contrast, raising the external pH from 5.8 to 7.0 increased [pH]cyt, while salt stress had no further increasing effects (Supplementary Fig. 12). Together, these results are in line with the chemical pH dependence of PA protonation and suggest that pH micro-environments in *Arabidopsis* cells affect the efficiency of PA to bind to its effector proteins and, in this way, may fine-tune the bioactivity of PA in response to environmental cues.

Although this postulated mechanism as cause for the observed $\Delta R/R_0$ decrease appears likely, we could not exclude a decrease of PA generation at the PM as an alternative mechanism. To further specify the underlying mechanism, we determined the influence of

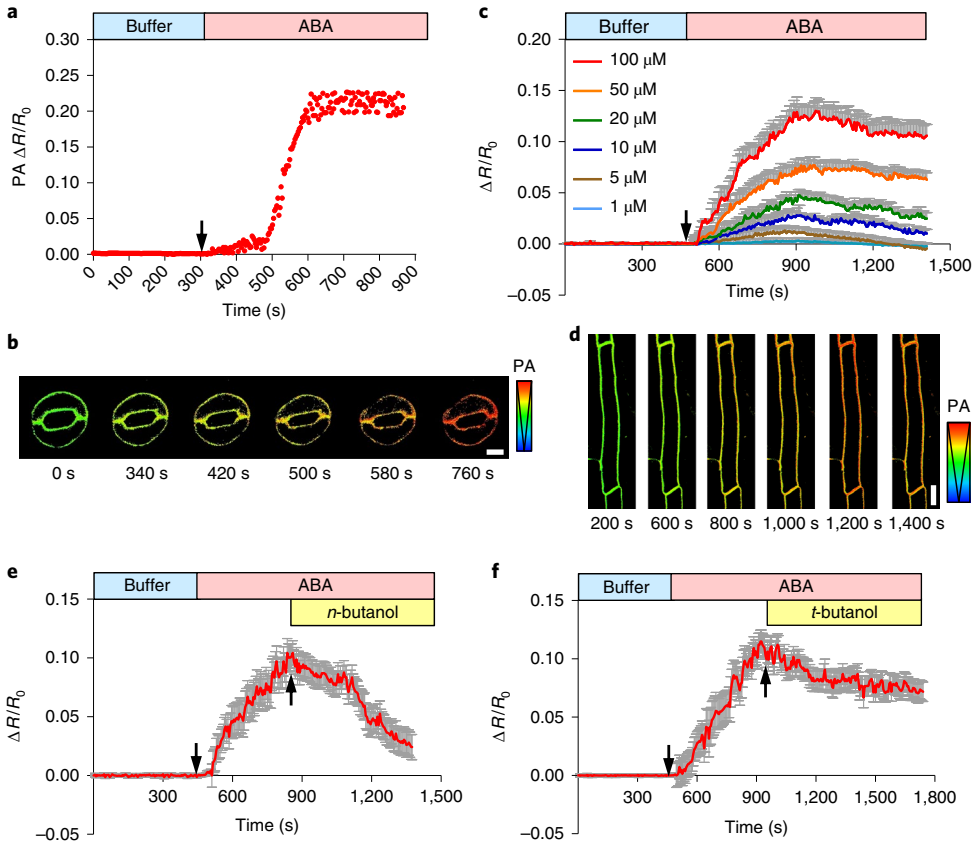

Fig. 3 | PA generation at the PM on ABA stimulation. a, PA accumulation at the PM of guard cells is induced by 100 μM ABA in WT seedlings expressing PAleon. **b**, Representative FRET images of cells from **a**. Scale bar, 5 μm. **c**, ABA at different concentrations induces PA accumulation at the PM of maturation zones in WT roots. **d**, Representative FRET images from **c**, in which the cells were treated with 100 μM ABA. Scale bar, 20 μm. **e**,**f**, Butanol effects on PA accumulation induced by 100 μM ABA. At the beginning of maximal PA accumulation, 0.4% *n*-butanol (**e**) or 0.4% *t*-butanol (**f**) was added. The data in **a** are representative determination of 20 stomata from 20 biologically independent seedlings with similar results. The data in **c**, **e** and **f** are mean ± s.e. from the determination of $n = 15$ (**c**), $n = 12$ (**e**) and $n = 14$ (**f**) cells for each seedling and a total of $n = 6$ biologically independent seedlings were tested for each treatment in one experiment. Three independent experiments were done with similar results. The arrows indicate the addition of ABA and/or butanols respectively.

PA protonation on its binding with R250 in vitro. The results showed that increasing H^+ in solution (lowering pH) reduced PA binding to R250 (Supplementary Fig. 13a). However, once PA had bound with R250 protein, environmental pH could not further modulate this binding (Supplementary Fig. 13b).

We next stimulated PLD activity by exposing *Arabidopsis* seedlings to salt stress, which is known to induce PA accumulation, to investigate if this PA accumulation would be sufficient to counteract PA protonation for ensuring the biological effectiveness of the PA response. In contrast to the FRET decrease induced by solely lowering pH in the media (Fig. 6c), when a seedling was simultaneously treated with low pH and NaCl, a rapid and prominent FRET increase was observed, followed by its decline (Fig. 6e). After readjustment of pH from 4.5 to 5.8 in the presence of NaCl, a second FRET peak appeared, although lower than the first peak (Fig. 6e). We reasoned that this second peak was caused by de-protonated PA; this would imply that a further increase of pH would also induce further de-protonation of PA and consequently result in a further increase of the FRET value. To test this, we performed another experiment in which a seedling was exposed to NaCl with pH 7.0. The treatment did cause a higher FRET peak ($\Delta R/R_0 \approx 0.45$; Fig. 6f), than that with pH 7.0 alone ($\Delta R/R_0 \approx 0.3$; Fig. 6d) or NaCl alone (pH 5.8; $\Delta R/R_0 \approx 0.2$; Fig. 5a). In the presence of NaCl, the change of pH from 7.0 to 5.8 led to a FRET decrease, and recovered completely after pH was re-changed to 7.0. The results suggest that the observed pH-induced FRET changes were reversible and also that the sensor structure remained stable under these conditions (Fig. 6f).

Together, these results uncover an integration of cellular pH dynamics with PA signalling in salt stress responses. This suggests that both salt-induced PLD activation (PA generation at PM) and pH changes (which probably affects protonation or de-protonation in cells) affect the detected FRET values indicative for PA accumulation.

Discussion

PA constitutes about 1% of total membrane glycerolipids in plants but its level changes dramatically on various stresses[3]. The complexity of intracellular distribution, trafficking, production and metabolism of PA has so far hampered our understanding of PA signalling, especially in plants. PA biosensors that would demonstrate PA dynamics in vivo have been developed in different organisms. Although Spo20p-derived translocation-based PA sensors have been used to show PA dynamics in living cells both in yeast and plants[17,19], most mechanistic facets of PA dynamics and function in plants remained to be determined.

In this study, we developed a genetically encoded FRET-based PA biosensor PAleon that allowed spatio-temporal and digital monitoring of PA dynamics in response to ABA and salt stress. The R250 module that we selected as PA-binding domain for PAleon has a high affinity to PAs, showing a K_d of ~2.3 μM (Fig. 1c),

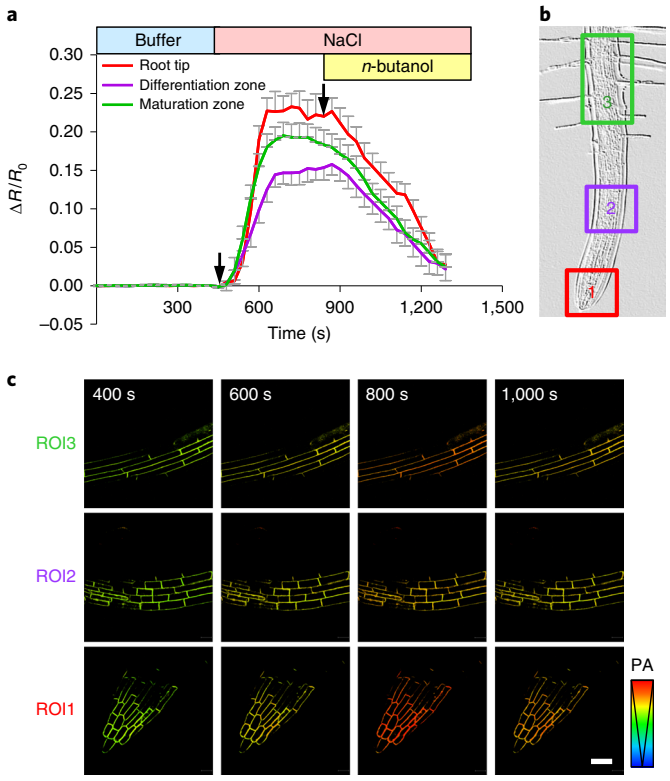

Fig. 4 | PA changes in root zones in response to salt stress. a, Salt stress induces PA accumulation at the PM in root zones. The seedlings were treated with 100 mM NaCl. The cells of three zones (indicated in **b**) in roots were determined for PA dynamics. After $\Delta R/R_0$ reached a plateau in terms of speed, 0.4% *n*-butanol was added. Data are reported as mean ± s.e. from the determination of $n = 10$ cells (for each zone) per seedling and on average three seedlings were tested in one experiment. Seven independent experiments were repeated with similar results. The arrows indicate the addition of NaCl or *n*-butanol, respectively. **b**, Schematic representation of ROIs encompassing root tip (ROI 1), differentiation zone (ROI 2) and maturation zone (ROI 3). **c**, Representative FRET ratio images of roots from **a**. Scale bar, 20 μm.

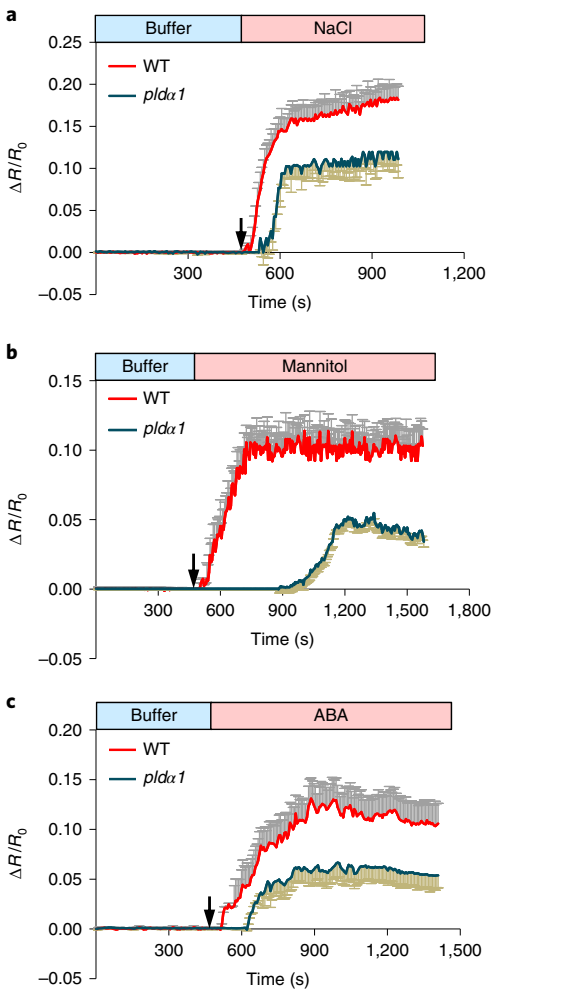

Fig. 5 | Loss of PLDα1 function impairs PA accumulation at the PM of roots exposed to stress. a–c, PA accumulation at the PM of maturation zones in WT and *pldα1* is affected differently by 100 mM NaCl (**a**), 200 mM mannitol (**b**) and 100 μM ABA (**c**). The data in **a–c** are shown as mean ± s.e. from $n = 13$ (**a**), $n = 15$ (**b**) and $n = 16$ (**c**) cells for each seedling and a total of $n = 5$ biologically independent seedlings for each genotype. Three independent experiments were done with similar results. The arrows indicate the addition of NaCl, mannitol or ABA.

which is a suitable sensitivity for monitoring PA concentrations in *Arabidopsis* cells[26]. The PAleon biosensor expressed in transgenic plants displayed a high specificity for physiologically relevant PA species in a concentration-dependent manner (Fig. 2 and Supplementary Fig. 6). In root tissues and guard cells, PAleon reported a rapidly induced accumulation of PA in response to salt stress and/or ABA. In addition, this biosensor had no obvious impact on the endogenous signalling system, as the expression of PAleon did not affect normal growth and stress responses (Supplementary Fig. 5). Taken together, our sensor characterization shows that PAleon is a suitable genetically encoded FRET biosensor for monitoring the spatio-temporal dynamics of PA at the PM in various cells and tissues with high specificity and sensitivity.

Using the PAleon biosensor, PA increases were observed in response to ABA in 1–2 min (Fig. 3). This reaction kinetics is comparable to that of ABA sensors to exogenously applied ABA[32,33], suggesting an immediate accumulation of PA on increase of cellular ABA concentration. Remarkably, compared with ABA responses, PA increased even more quickly in response to NaCl and mannitol treatments (Fig. 5). In this way, the PAleon biosensor most likely reflects differences in the uptake and function of both stimuli: (1) ABA influx into cells (or onto PM) takes longer than osmotic pressure generation by addition of NaCl or mannitol solution; (2) the osmotic pressures on cells could stimulate force-induced mixing of lipid compartments (or micro-domains) with mechanosensitive proteins (for example, PLD) in the PM[34,35]. In fact, PLD has been established to experience increased access to its substrates (for example, PC) during the remodulation of membrane micro-domains in mouse cells, which results in PA increase[34]. Compared with the ABA-induced PLD activation that probably occurs via ABA receptors and G proteins[36], the PLD activation induced by immediate remodulation of PM micro-domains could occur more directly and faster. Moreover, the C-terminal region of K-Ras4B, here used as a PM-anchor for the PAleon, has previously been used to anchor the pH sensor pHluorin to the PM–cytoplasm interface[37], and PA was found to accumulate in the region of the PM cytosolic leaflet in tobacco pollen tubes[19] and *Arabidopsis* roots[37]. Remarkably, the PM-anchoring region of K-Ras4B contains a farnesylation signal and farnesylated proteins are likely to be associated with PM micro-domains[38]. Thus, it would be of interest in future studies to determine whether the PAleon is partitioned into defined PM micro-domains.

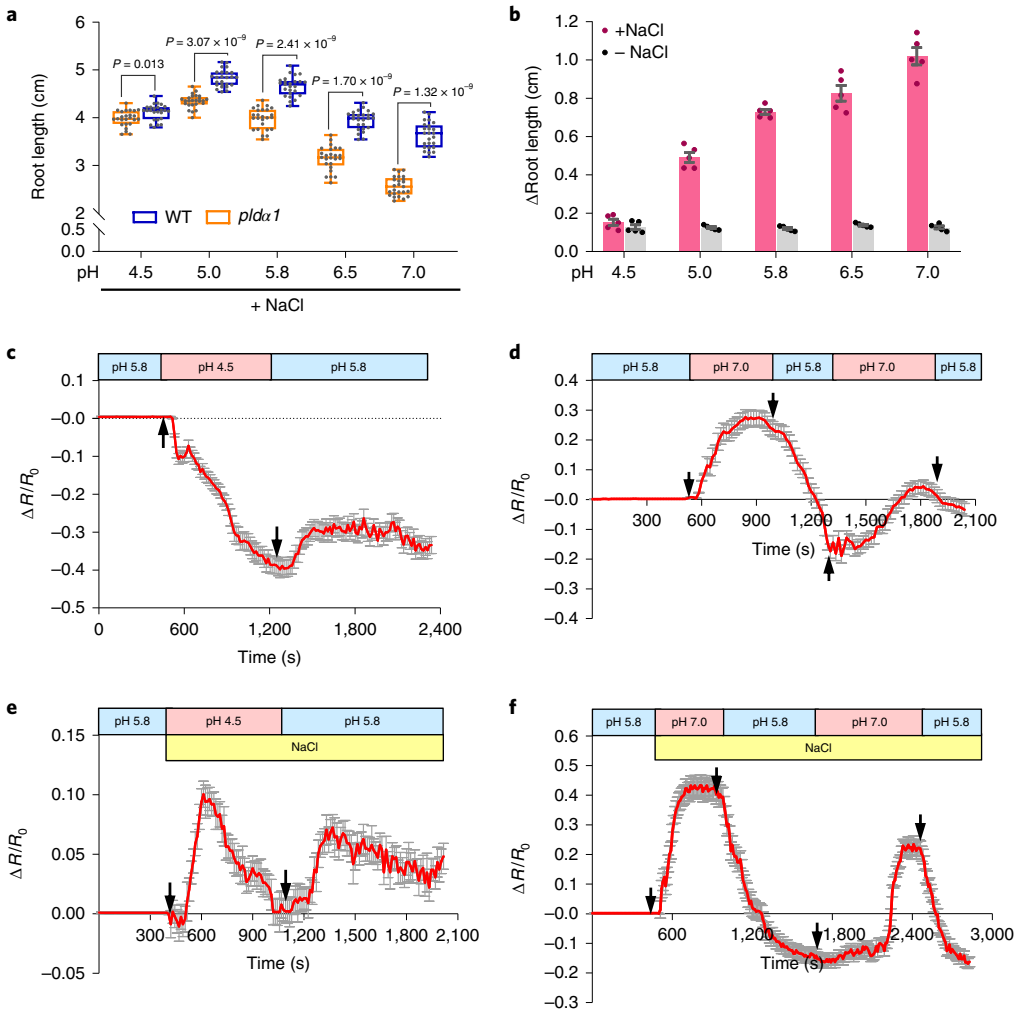

Fig. 6 | Interconnection between PA and pH homoeostasis in salt response. a, Root growth: 3-day-old seedlings grown on one-half MS medium were transferred to one-half MS medium containing 100 mM NaCl with a different pH for 10 d and root length was determined. **b**, Combined effects of PLDα1 and pH on root growth under salt stress. The data are shown as difference of root length (WT minus *pldα1*) according to **a** with NaCl and without NaCl (Supplementary Fig. 10b). **c**, Lower pH (pH 4.5) stimulation induces a decrease of FRET. **d**, Higher pH (pH 7.0) stimulation induces an increase of FRET. **e**, Combined effects of lower pH and salt stress (100 mM NaCl) on FRET. **f**, Combined effects of higher pH and salt stress on FRET. The data in **a** and **b** are from the determination of $n = 25$ biologically independent seedlings for each genotype per treatment. Five independent experiments were done with similar results. In the box plots shown in **a**, the boxes indicate the first and third quartiles and the whiskers indicate the minimum to maximum values. The lines within the boxes indicate the median values. Statistically significant differences were determined by the two-tailed Mann–Whitney–Wilcoxon test. The representative results from one experiment are shown. The data in **b** represent means ± s.e. from the median values of **a** with five independent experiments. The data in **c–f** represent mean ± s.e. from $n = 11$ (**c**), $n = 14$ (**d**), $n = 17$ (**e**) and $n = 10$ (**f**) cells for each seedling and five biologically independent seedlings for each experiment. Four independent experiments were done with similar results.

By the application of the PAleon biosensor, we revealed at genetic and cellular levels that PLDα1 contributes to stress-induced PA production at the PM, and that the PLDα1-derived PA changes differ in distinct plant tissues on stimulation. Previous studies on *pldα1* mutant plants had indicated the functional importance of PLD in plant salt tolerance and guard cell regulation[7,8,15,23]. When plants were challenged with NaCl, mannitol or ABA, we observed striking differences in the accumulation of PA in the *pldα1* mutant when compared to WT (Fig. 5). This provides further in vivo evidence for the reliability of the PAleon biosensor. Moreover, we uncovered noticeable differences in the kinetic and quantitative consequences of PA changes from *pldα1* loss among the stress conditions investigated. These findings indicate that PLDα1 contributes PA production differently under different stress conditions. Moreover, this may also suggest that different regulatory mechanisms determine the activation of this enzyme in different physiological processes.

In addition, results here indicate that pH changes in plant cells affect PA signalling by modulating the protonation and de-protonation of PA and thereby its target binding. The pH homeostasis is essential for cellular functions. In *Arabidopsis*, the PM pH gradient gradually increases from the surface of the root to the stele[37]. Since numerous transporter and channel activities are regulated by the PM pH gradient across these cells probably contributes to the uptake of minerals from root surface to the stele[37]. In yeast, pH-modulated PA target binding allows for its function as a pH biosensor, coupling changes in pH to intracellular nutrient signalling[2]. Here we showed not only that the PAleon–PA interaction, thus PA detection, is influenced by pH changes but also that decreased pH diminished the effect of PLDα1 on salt tolerance whereas increasing the medium pH enhanced the PLDα1 effect (Fig. 6). Thus the salt stress response provides a unique system to illustrate the interdependence of pH homeostasis and PA signalling in plant cells. The PM H^+-ATPase

activation by salt stress pumps H^+ out of the cell, generating an H^+ gradient across the PM to provide the force for Na^+/H^+ antiport and inducing an alkaline micro-environment at the inner PM[39,40]. It thus creates a higher propensity for PA to bind effectors thereby facilitating efficiency of PA signalling. Both PM H^+-ATPase and PLDα1 activation were found to occur in *Arabidopsis* in response to salt stress[25,41]. As a result, a PA effector, MPK6 (mitogen-activated protein kinase 6) is bound and activated by salt-induced PA in the WT but not in *pldα1* cells in which PA was not increased[25]. Moreover, MPK6 phosphorylates the Na^+/H^+ antiporter SOS1 (salt overly sensitive 1), at least in vitro[25], which centrally functions in plant salt tolerance by pumping Na^+ out of the cell to reduce its toxicity and H^+ back into cytosol. In this way, continuing Na^+ extrusion would result in cellular acidification, which would reduce efficiency of PA target binding, thereby providing a feedback mechanism for fine-tuning PA signalling. On the other hand, among the 12 members of the *Arabidopsis* PLD family, at least PLDα1, PLDα3 and PLDδ, which display different sensitivities to pH[42], have been found to positively regulate salt tolerance[15,25,43]. It is therefore tempting to suggest, that the pH-dependent activation of many PLDs in turn could provide a compensatory mechanism to counteract the unfavourable effects of media/soil acidification by SOS1 activity. Notably, Ca^{2+}-signalling functions in the activation of SOS1 Na^+/H^+ antiport activity. It has been established that fluctuations of Ca^{2+} concentration usually coincide with pH value fluctuations in cells during salt stress and in many physiological processes[30,34,40]. Consequently, we propose that Ca^{2+}-signalling in combination with pH-modulated PA effector binding provides a core mechanism for signal integration during plant responses to salt stress.

In summary, our work demonstrates that PAleon monitors dynamic changes in PA concentrations at the PM in diverse tissues and cell types in response to stress conditions. Using this biosensor, we reveal that PA signalling couples with cellular pH to determine *Arabidopsis* tolerance to salt stress. Since PA signalling also occurs in the membranes of plastids, endoplasmic reticulum and nuclei, our work paves the way for building specifically targeted synthetic signalling sensors for these compartments to further explain important facets of subcellular PA dynamics and functions.

Methods

Plant materials and growth. *Arabidopsis thaliana* plants used in this study were from the Columbia ecotype. Seeds were plated on one-half Murashige and Skoog (MS) medium (pH 5.8) supplemented with 0.1% (w/v) sucrose and solidified with 1% (w/v) agar. After germinating at 4 °C in the dark for 2 d, seedlings were vertically grown for 3–4 d under 12 h/12 h (23 °C/18 °C) day/night regimes of light intensity of 160 μmol m^{-2} s^{-1}. These seedlings (~1 cm of roots) were used for confocal microscopy analysis. Plants of 4–6 weeks old, grown in soil under the same conditions, were used to prepare protoplasts and epidermal peels.

Plasmid construction for PAleon. PAleon construction was modified from Pii reported by Nishioka et al.[24]. It consisted of CFP (1-237 amino acids), six repeats of Glu-Ala-Ala-Ala-Arg amino acid sequences, R250 (1–250 amino acids from RbohD protein), a spacer Glu-Ala-Ala-Ala-Arg-Glu-Ala-Ala-Ala-Arg-Glu-Ala-Ala-Ala-Arg-Gly-Gly-Glu-Ala-Ala-Ala-Arg-Glu-Ala-Ala-Ala-Arg-Glu-Ala-Ala-Ala-Arg, VENUS (1-237 amino acids), seven repeats of Glu-Ala-Ala-Ala-Arg amino acid sequences and the C-terminal region of K-Ras4B (169–188 amino acids). The negative control was the R250M, which mutated R250D with quadruple mutation Arg(149,150,156,157)Ala in RbohD[7].

Transgenic plants. Coding sequences of PAleon were digested with HindIII and ApaI restriction enzymes and ligated into the modified constitutive binary vector with octopine synthase and mannopine synthase promoters[27]. The binary vectors were then introduced into the *Agrobacterium tumefaciens* GV3101 strain that was used to generate transgenic *Arabidopsis* plants by floral dip. For each construct, 20 independent transgenic *Arabidopsis* lines were selected and seven independent lines were used for imaging experiments. Experiments were carried out in seedlings of the T_3 generation for PAleon transgenic lines.

Dynamic PA imaging using confocal microscopy analysis. A 4-day-old seedling was loaded in a dedicated chamber and overlaid with wet cotton to continuously perfuse the root with the imaging buffer (5 mM KCl, 10 mM Ca^{2+}, 10 mM MES–Tris, pH 5.8) as reported previously[44] or other buffer indicated in the text. PA dynamic was recorded by a spinning confocal disc (Perkin–Elmer). The CFP (excitation 440 nm/emission 475 nm) and FRET (excitation 440 nm/emission 535 nm) signals were recorded, respectively. The background was subtracted independently for both channels before calculating the ratio. For time-course experiments, fluorescence intensity was determined over ROI that correspond to single cell in root or guard cells. FRET and CFP emissions of the analysed ROI were used for the ratio (R) calculation (FRET/CFP) and normalized to the initial ratio (R_0) and plotted versus time ($\Delta R/R_0$).

To determine salt-induced PA dynamics in different zones of a root simultaneously, images were acquired with 'XY-plane' mode. Three zones, that is root tip, differentiation and maturation, were selected as 'added points' in XY-plane mode. The images in the three zones from a PAleon transgenic plant could be obtained at almost the same time (less than 2 s from one zone to the next zone). Considering the osmotic effects caused by NaCl (or mannitol) on cell shapes and PAleon fluorescent intensity, three-dimensional images were acquired using 'three-dimensional' mode over the ROI. Each ROI was scanned with four slices for every time point and extended as one image. For PA imaging analysis, the false colour ratio images were obtained by using the Volocity bundle software.

Unless indicated in the figure legend, we selected the cells in maturation zone of roots for FRET analysis. The statistical significance was calculated by Student's t-test.

To compare spatial patterns, subcellular localization images were performed with Zeiss LSM780 confocal laser scanning microscope (Zeiss Microsystems) equipped with ×20 numerical aperture objectives. Excitation/emission wavelengths were: CFP, 440 nm /450–480 nm; FRET, 440 nm /520–570 nm; FM4-64, 561 nm (diode-pumped solid-state laser) /570–635 nm. Multi-colour imaging of cells co-expressing PAleon and FM4-64 was performed by sequential scanning to prevent crosstalk.

Expression and purification of fusion proteins. The coding regions of RbohD fragment R250 and its quadruple mutant R250M were amplified by PCR and digested with BamHI and XhoI and cloned into the pET-28a(+) vector. Recombinant plasmids carrying R250(M) with six histidine residues were transformed into *Escherichia coli* BL21 (DE3). The protein expression and purification were carried out as previously[7].

Isothermal titration calorimetry. Thermodynamic parameters of molecular interactions between R250(M) and PA were investigated by isothermal titration calorimetry[6], using MicroCal ITC-200 calorimeter (General Electric Company). The protein and PA were equilibrated in buffer containing 50 mM HEPES, 50 mM NaCl and 50 mM KCl. The final concentration of R250(M) was adjusted to 1 μM. The PA concentration used was 10 μM. The R250(M) in a calorimeter cell was titrated by a series of automatic injections of 2 μl PA each. Integration of the peaks corresponding to each injection and correction for the baseline were done using Origin-based software provided by the manufacturer. All experiments were repeated three times and gave similar results. Control experiments without R250(M) in calorimeter cell solution were performed to evaluate the heat of blank dilution. The results were analysed using the Origin software (MicroCal) from which the binding stoichiometry (N) and equilibrium dissociation constant (K_d) were determined by fitting a one-site model to the results.

Lipid–protein binding assay. Protein–lipid interaction was assayed using filter and ELISA approaches according to the previous methods[7] with minor modification. Briefly, lipid-binding activity was assessed on nitrocellulose filters or PIPs P6001 strips (Echelon Biosciences) with lipids immobilized. Each filter (strip) was incubated with 10 ml PBST containing the R250(M) protein (0.5 μg ml^{-1}) after 1 h of blocking. The protein was maintained overnight at 4 °C, then removed and the membrane was washed three times with PBST before adding 10 ml PBST containing anti-$(His)_6$ antibody (Sigma–Aldrich) from mouse (1:4,000 dilution). The filters (or trips) were then incubated with anti-mouse IgG antibody from goat (Sigma–Aldrich), followed by horseradish peroxidase (HRP) conjugation (1:5,000 dilution). The blot was activated by the addition of 1 ml of each component of the chemiluminescent substrate and exposed to film for 10 s.

To carry out ELISA-based assay, 2 μg 16:0–18:2 PA was coated on wells of 96-well titer plates. After chloroform evaporation from wells, pH buffer (PBS, 200 μl, pH 4.5–8.0) was added into wells and incubated for 4 h, followed by addition of $(His)_6$-R250 (20 μl, 4 μg) into each well and incubation for another 4 h. The buffer was then removed from wells and washed three times with PBST before adding anti-His antibody (Sigma–Aldrich) from mouse (1:2,000 dilution). This was followed by incubation with HRP-conjugated anti-mouse IgG antibody from goat (Sigma–Aldrich) (1:5,000 dilution) and optical density value was determined with spectrometric measurements by EL-TMB. To determine whether environmental pH still has effects after R250 has already been bound by PA, 2 μg of 16:0–18:2 PA was coated, 20 μl of R250(M) (4 μg, pH 7.4) was incubated in wells for 4 h, followed by addition of pH buffer (PBS, 200 μl, pH 4.5–8.0) and incubation for another 4 h. The addition of antibodies and optical density value determination were then done as above.

FRAP experiments. Confocal laser scanning imaging was performed with a Perkin–Elmer equipped with a ×20 objective. The CFP (excitation 440 nm/

emission 475 nm) and Venus (excitation 515 nm/emission 535 nm) signals were recorded, respectively. Five pre-bleach scans (one scan every 30 s) at 8% maximal laser power were used to determine initial fluorescence intensity, after which one photobleaching scan was executed at 100% laser power. Post-bleach fluorescence recovery was then sampled at 8% laser power for 90 s. Quantifications of FRAP were performed using confocal bundle software.

Measurement of cytosolic pH. Cytosolic pH was measured using the pH-sensitive dye BCECF-AM according to the methods of Wilkins et al.[31] with minor modification. Briefly, 4-day-old *Arabidopsis* seedlings were incubated in image buffer containing 10 µM BCECF-AM 0.02% pluronic F-127 (Molecular Probes) for 15 min in darkness at 22 °C and were washed twice using image buffer before observation under microscopy. Dye fluorescence images were collected using a Perkin–Elmer spinning disc confocal microscope equipped with a ×20 objective after excitation with 440 and 515 nm. Emission between 535 and 550 nm was collected for each excitation wavelength. Images were collected from root cells. Images were taken at each of the following pH values to create a calibration curve: pH 5.5, pH 6.0, pH 6.5, pH 7.0, pH 7.5 and pH 8. These ratios were plotted to give a calibration curve to pH ratio that was used to calculate the pH of individual root cells after various treatments.

PAO treatment and dissociation index. Four-day-old PAleon transgenic *Arabidopsis* seedlings were treated with 60 µM PAO (Sigma, PAO stock solution at 60 mM in DMSO). The dissociation index was measured according to the method described by Simon et al.[28]. Briefly, roots were imaged every 10 min and the PAO effects on the localization of PAleon were analysed by calculating the 'dissociation index' for each reporter protein. We first measured the $index_{mock}$, the ratio between the fluorescence intensity measured in two ROIs from the PM region (one at the apical/basal PM region and one in the lateral PM region) and two ROIs in the cytosol, in the mock condition. Next, we measured a similar ratio in PAO-treated seedlings ($index_{PAO}$). The dissociation index is the ratio of $index_{mock}/index_{PAO}$. This dissociation index reveals the degree of relocalization of the fluorescent reporters from the PM to the cytosol.

Reporting Summary. Further information on research design is available in the Nature Research Reporting Summary linked to this article.

Data availability

The data that support the findings of this study are available within the paper and its Supplementary Information or from the corresponding authors upon request.

Received: 10 August 2018; Accepted: 27 June 2019;
Published online: 26 August 2019

References

1. Pokotylo, I., Kravets, V., Martinecc, J. & Ruelland, E. The phosphatidic acid paradox: too many actions for one molecule class? Lessons from plants. *Prog. Lipid Res.* **71**, 43–53 (2018).
2. Young, B. P. et al. Phosphatidic acid is a pH biosensor that links membrane biogenesis to metabolism. *Science* **329**, 1085–1088 (2010).
3. Wang, X., Su, Y., Liu, Y., Kim, S. C. & Fanella, B. *Signaling and Communication in Plants* (ed. Wang, X.) 69–92 (Springer, 2014).
4. Kassas, N. et al. Comparative characterization of phosphatidic acid sensors and their localization during frustrated phagocytosis. *J. Biol. Chem.* **292**, 4266–4279 (2017).
5. Jacob, T., Ritchie, S., Assmann, S. & Gilroy, S. Abscisic acid signal transduction in guard cells is mediated by phospholipase D activity. *Proc. Natl Acad. Sci. USA* **96**, 12192–12197 (1999).
6. Mishra, G., Zhang, W., Deng, F., Zhao, J. & Wang, X. A bifurcating pathway directs abscisic acid effects on stomatal closure and opening in *Arabidopsis*. *Science* **312**, 264–266 (2006).
7. Zhang, Y. et al. Phospholipase Dα1 and phosphatidic acid regulate NADPH oxidase activity and production of reactive oxygen species in ABA-mediated stomatal closure in *Arabidopsis*. *Plant Cell* **21**, 2357–2377 (2009).
8. Zhang, Q. et al. Phosphatidic acid regulates microtubule organization by interacting with MAP65-1 in response to salt stress in *Arabidopsis*. *Plant Cell* **24**, 4555–4576 (2012).
9. Galvan-Ampudia, C. S. et al. Halotropism is a response of plant roots to avoid a saline environment. *Curr. Biol.* **23**, 2044–2050 (2013).
10. Wang, P. et al. Phosphatidic acid directly regulates PINOID-dependent phosphorylation and activation of the PIN-FORMED 2 auxin efflux transporter in response to salt stress. *Plant Cell* **31**, 250–271 (2019).
11. McLoughlin, F. et al. The Snf1-related protein kinases SnRK2.4 and SnRK2.10 are involved in maintenance of root system architecture during salt stress. *Plant J.* **72**, 436–449 (2012).
12. Testerink, C. & Munnik, T. Molecular, cellular, and physiological responses to phosphatidic acid formation in plants. *J. Exp. Bot.* **62**, 2349–2361 (2011).
13. Welti, R. et al. Profiling membrane lipids in plant stress responses. Role of phospholipase Dα in freezing-induced lipid changes in *Arabidopsis*. *J. Biol. Chem.* **277**, 31994–32002 (2002).
14. Shadyro, O., Yurkova, I., Kisel, M., Brede, O. & Arnhold, J. Formation of phosphatidic acid, ceramide, and diglyceride on radiolysis of lipids: identification by MALDI-TOF mass spectrometry. *Free Radic. Biol. Med.* **36**, 1612–1624 (2004).
15. Bargmann, B. O. R. et al. Multiple PLDs required for high salinity and water deficit tolerance in plants. *Plant Cell Physiol.* **50**, 78–89 (2009).
16. An, N., Rudge, S. A., Zhang, Q. & Wakelam, M. J. Using lipidomics analysis to determine signalling and metabolic changes in cells. *Curr. Opin. Biotech.* **43**, 96–103 (2017).
17. Nakanishi, H., Santos, P. D. L. & Neiman, A. M. Positive and negative regulation of a SNARE protein by control of intracellular localization. *Mol. Biol. Cell* **15**, 1802–1815 (2004).
18. Rizzo, M. A., Shome, K., Watkins, S. C. & Romero, G. The recruitment of Raf-1 to membranes is mediated by direct interaction with phosphatidic acid and is independent of association with Ras. *J. Biol. Chem.* **275**, 23911–23918 (2000).
19. Potocký, M. et al. Live-cell imaging of phosphatidic acid dynamics in pollen tubes visualized by Spo20p-derived biosensor. *New Phytol.* **203**, 483–494 (2014).
20. Platre, M. P. et al. A combinatorial lipid code shapes the electrostatic landscape of plant endomembranes. *Dev. Cell* **45**, 465–480 (2018).
21. Tavare, J. M., Fletcher, L. M. & Welsh, G. I. Using green fluorescent protein to study intracellular signaling. *J. Endocrinol.* **170**, 297–306 (2001).
22. Wang, X., Devaiah, S. P., Zhang, W. & Welti, R. Signaling functions of phosphatidic acid. *Prog. Lipid Res.* **45**, 250–278 (2006).
23. Zhang, W., Qin, C., Zhao, J. & Wang, X. Phospholipase Dα1-derived phosphatidic acid interacts with ABI1 phosphatase 2C and regulates abscisic acid signaling. *Proc. Natl Acad. Sci. USA* **101**, 9508–9513 (2004).
24. Nishioka, T., Frohman, M. A., Matsuda, M. & Kiyokawa, E. Heterogeneity of phosphatidic acid levels and distribution at the plasma membrane in living cells as visualized by a Förster resonance energy transfer (FRET) biosensor. *J. Biol. Chem.* **285**, 35979–35987 (2010).
25. Yu, L. et al. Phosphatidic acid mediates salt stress response by regulation of MPK6 in *Arabidopsis thaliana*. *New Phytol.* **188**, 762–773 (2010).
26. Devaiah, S. P. et al. Quantitative profiling of polar glycerolipid species from organs of wild-type *Arabidopsis* and a phospholipase Dα1 knockout mutant. *Phytochemistry* **67**, 1907–1924 (2006).
27. Ni, M. et al. Strength and tissue specificity of chimeric promoters derived from the octopine and mannopine synthase genes. *Plant J.* **7**, 661–676 (1995).
28. Simon, M. L. et al. A PtdIns(4)P-deriven electrostatic field controls cell membrane identity and signaling in plants. *Nat. Plants* **2**, 16089–16098 (2016).
29. Waadt, R. et al. FRET-based reporters for the direct visualization of abscisic acid concentration changes and distribution in *Arabidopsis*. *eLife* **3**, e01739 (2014).
30. Behera, S. et al. Cellular Ca^{2+} signals generate defined pH signatures in plants. *Plant Cell* **30**, 2704–2719 (2018).
31. Wilkins, K. A. et al. Self-incompatibility-induced programmed cell death in field poppy pollen involves dramatic acidification of the incompatible pollen tube cytosol. *Plant Physiol.* **167**, 766–779 (2015).
32. Darwish, E., Testerink, C., Khalil, M., Elshihy, O. & Munnik, T. Phospholipid signaling responses in salt-stressed rice leaves. *Plant Cell Physiol.* **50**, 986–997 (2009).
33. Jones, A. M. et al. Abscisic acid dynamics in roots detected with genetically encoded FRET sensors. *eLife* **3**, e01741 (2014).
34. Petersen, E. N., Chung, H. W., Nayebosadri, A. & Hansen, S. B. Kinetic disruption of lipid rafts is a mechanosensor for phospholipase D. *Nat. Commun.* **7**, 13873 (2016).
35. Basu, D. & Haswell, E. S. Plant mechanosensitive ion channels: an ocean of possibilities. *Curr. Opin. Plant Biol.* **40**, 43–48 (2017).
36. Zhao, J. & Wang, X. *Arabidopsis* phospholipase Dα1 interacts with the heterotrimeric G-protein α-subunit through a motif analogous to the DRY motif in G-protein-coupled receptors. *J. Biol. Chem.* **279**, 1794–1800 (2004).
37. Martinière, A. et al. Uncovering pH at both sides of the root plasma membrane interface using noninvasive imaging. *Proc. Natl Acad. Sci. USA* **115**, 6488–6493 (2018).
38. Rocks, O., Peyker, A. & Bastiaens, P. I. H. Spatio-temporal segregation of Ras signals: one ship, three anchors, many harbors. *Curr. Opin. Cell Biol.* **18**, 351–357 (2006).
39. Munns, R. & Tester, M. Mechanisms of salinity tolerance. *Annu. Rev. Plant Biol.* **59**, 651–681 (2008).
40. Yang., Y. & Guo, Y. Elucidating the molecular mechanisms mediating plant salt-stress responses. *New Phytol.* **217**, 523–539 (2018).

41. Gevaudant, F. et al. Expression of a constitutively activated plasma membrane H^+-ATPase alters plant development and increases salt tolerance. *Plant Physiol.* **144**, 1763–1776 (2007).
42. Wang, X. Multiple forms of phospholipase D in plants: the gene family, catalytic and regulatory properties, and cellular functions. *Prog. Lipid Res.* **39**, 109–149 (2000).
43. Hong, Y., Pan, X., Welti, R. & Wang, X. Phospholipase Dα3 is involved in the hyperosmotic response in *Arabidopsis*. *Plant Cell* **20**, 803–816 (2008).
44. Krebs, M. et al. FRET-based genetically encoded sensors allow high-resolution live cell imaging of Ca^{2+} dynamics. *Plant J.* **69**, 181–192 (2012).

Acknowledgements

We thank E. Kiyokawa (Department of Pathology and Biology of Diseases, Graduate School of Medicine, Kyoto University) for the generous gift of the Pii vector. We thank J. Chen and X. Liu for their assistance in using confocals. The research was supported by grants from National Natural Science Foundation of China (grant nos. 31770294 and 31570270) to W.Z. and from the Deutsche Forschungsgemeinschaft (grant no. DFG, KU931/14-1).

Author contributions

W.L. and W.Z. designed experiments, analysed data and wrote the manuscript. W.L. performed most of the experiments and prepared the data. T.S. and L.W. helped with the experiments. J.K., L.W. and X.W. discussed the data and revised the manuscript.

Competing interests

The authors declare no competing interests.

Additional information

Supplementary information is available for this paper at https://doi.org/10.1038/s41477-019-0497-6.

Reprints and permissions information is available at www.nature.com/reprints.

Correspondence and requests for materials should be addressed to W.Z.

Publisher's note: Springer Nature remains neutral with regard to jurisdictional claims in published maps and institutional affiliations.

nature research

Corresponding author(s): Wenhua Zhang

Last updated by author(s): Jun 12, 2019

Reporting Summary

Nature Research wishes to improve the reproducibility of the work that we publish. This form provides structure for consistency and transparency in reporting. For further information on Nature Research policies, see Authors & Referees and the Editorial Policy Checklist.

Statistics

For all statistical analyses, confirm that the following items are present in the figure legend, table legend, main text, or Methods section.

n/a	Confirmed
☐	☒ The exact sample size (*n*) for each experimental group/condition, given as a discrete number and unit of measurement
☐	☒ A statement on whether measurements were taken from distinct samples or whether the same sample was measured repeatedly
☐	☒ The statistical test(s) used AND whether they are one- or two-sided *Only common tests should be described solely by name; describe more complex techniques in the Methods section.*
☒	☐ A description of all covariates tested
☒	☐ A description of any assumptions or corrections, such as tests of normality and adjustment for multiple comparisons
☐	☒ A full description of the statistical parameters including central tendency (e.g. means) or other basic estimates (e.g. regression coefficient) AND variation (e.g. standard deviation) or associated estimates of uncertainty (e.g. confidence intervals)
☐	☒ For null hypothesis testing, the test statistic (e.g. *F*, *t*, *r*) with confidence intervals, effect sizes, degrees of freedom and *P* value noted *Give P values as exact values whenever suitable.*
☒	☐ For Bayesian analysis, information on the choice of priors and Markov chain Monte Carlo settings
☒	☐ For hierarchical and complex designs, identification of the appropriate level for tests and full reporting of outcomes
☒	☐ Estimates of effect sizes (e.g. Cohen's *d*, Pearson's *r*), indicating how they were calculated

Our web collection on statistics for biologists contains articles on many of the points above.

Software and code

Policy information about availability of computer code

Data collection	ZEISS LSM780 software was used to collect subcellular localization figures; PerkinElmer Volocity bundle software from spinning disc confocal was used to collect figures and data of PA, FRAP and pH dynamics; Microcal ITC_200 calorimeter software for lipid-protein binding assay; Tanon 5200 software for Western blot and Fat blot; Tecan Magellan software was used for ELISA assay
Data analysis	PerkinElmer Volocity bundle software was used to analyze FRET and FRAP;Microsoft Excel 2010, and GraphPad Prism were used to analyze the data ; Powerpoint was used for Figure assembly. Western blots was created as shown; Image J was used to analyze root length; Origin-based software was used to analyze ITC data

For manuscripts utilizing custom algorithms or software that are central to the research but not yet described in published literature, software must be made available to editors/reviewers. We strongly encourage code deposition in a community repository (e.g. GitHub). See the Nature Research guidelines for submitting code & software for further information.

Data

Policy information about availability of data

All manuscripts must include a data availability statement. This statement should provide the following information, where applicable:

- Accession codes, unique identifiers, or web links for publicly available datasets
- A list of figures that have associated raw data
- A description of any restrictions on data availability

The authors declare that all data supporting the findings of this study are available within the paper and its supplementary information, or from the corresponding author on request.

Field-specific reporting

Please select the one below that is the best fit for your research. If you are not sure, read the appropriate sections before making your selection.

☒ Life sciences ☐ Behavioural & social sciences ☐ Ecological, evolutionary & environmental sciences

For a reference copy of the document with all sections, see nature.com/documents/nr-reporting-summary-flat.pdf

Life sciences study design

All studies must disclose on these points even when the disclosure is negative.

Sample size	Statistical analysis was made in Fig.6 by two-tailed Mann-Whitney-Wilcoxon test. For other figures, the sample sizes were determined based on the previous reports and were sufficient for reproducible results.
Data exclusions	No data were excluded from our analyses.
Replication	For each experiment, the experimental findings were reliably reproduced. At least, three times these experiments were repeated independently with similar results.
Randomization	In the case of comparing different genotypes and different treatments, seedlings were grown randomly in a growth chamber.
Blinding	Most experiments were not blinding because they were chemical treatments, in which the fluorescence changes were recorded by confocal. Key results were observed by two investigators. Root growth was measured being unaware of the genotype analyzed.

Reporting for specific materials, systems and methods

We require information from authors about some types of materials, experimental systems and methods used in many studies. Here, indicate whether each material, system or method listed is relevant to your study. If you are not sure if a list item applies to your research, read the appropriate section before selecting a response.

Materials & experimental systems

n/a	Involved in the study
☐	☒ Antibodies
☒	☐ Eukaryotic cell lines
☒	☐ Palaeontology
☒	☐ Animals and other organisms
☒	☐ Human research participants
☒	☐ Clinical data

Methods

n/a	Involved in the study
☒	☐ ChIP-seq
☒	☐ Flow cytometry
☒	☐ MRI-based neuroimaging

Antibodies

Antibodies used	Antibodies used in Western blotting and Fat blotting were purchased from the commercial supplier Sigma-Aldrich: Anti-polyHistidine antibody from mouse (Sigma-Aldrich, Catalog code:H1029, clone: HIS-1, monoclonal, primary antibodies, dilution 1:4000). Anti-mouse IgG antibody from goat (Sigma-Aldrich, Catalog code: A4416, clone: polyclonal, secondary antibodies, dilution 1:5000).
Validation	Anti-His (Sigma-Aldrich H1029) and anti-mouse IgG (Sigma-Aldrich A4416) antibodies have been validated by the manufacturer. Validation statements for the antibodies can be found on manufacturers' websites (https://www.sigmaaldrich.com/catalog/product/sigma/h1029?lang=zh&region=CN; https://www.sigmaaldrich.com/catalog/product/sigma/a4416?lang=zh&region=CN) . The antibodies were also validated by published papers (e.g. Imbert et al. EMBO J 2017, 36: 1869-1887).